JGR Solid Earth

RESEARCH ARTICLE
10.1029/2020JB019518

Key Points:

- We assess techniques for magnetic unmixing of complex hematite and magnetite mixtures in red chert
- Domain state and coercivity distributions of mixtures in red chert are best characterized using a combination of unmixing techniques
- Principal component analysis is suitable for assessing large sample sets; IRM and FORC unmixing provide component-specific identifications

Supporting Information:

- Supporting Information S1

Correspondence to:
P. Hu,
pengxiang.hu@anu.edu.au

Citation:
Hu, P., Oda, H., Zhao, X., Harrison, R. J., Heslop, D., Sato, T., et al. (2021). Assessment of magnetic techniques for understanding complex mixtures of magnetite and hematite: The Inuyama red chert. *Journal of Geophysical Research: Solid Earth*, *126*, e2020JB019518. https://doi.org/10.1029/2020JB019518

Received 13 FEB 2020
Accepted 25 NOV 2020

Assessment of Magnetic Techniques for Understanding Complex Mixtures of Magnetite and Hematite: The Inuyama Red Chert

Pengxiang Hu[1,2], Hirokuni Oda[1], Xiang Zhao[1,2], Richard J. Harrison[3], David Heslop[1,2], Tetsuro Sato[1], Adrian R. Muxworthy[4], and Andrew P. Roberts[1,2]

[1]Research Institute of Geology and Geoinformation, Geological Survey of Japan, National Institute of Advanced Industrial Science and Technology (AIST), AIST Tsukuba Central 7, Tsukuba, Ibaraki, Japan, [2]Research School of Earth Sciences, Australian National University, Canberra, ACT, Australia, [3]Department of Earth Sciences, University of Cambridge, Cambridge, UK, [4]Department of Earth Science and Engineering, Imperial College London, South Kensington Campus, London, UK

Abstract Magnetite and hematite mixtures occur widely in nature. Magnetic unmixing of the signals recorded by these minerals can be important for assessing the origin of their respective paleomagnetic remanences and for extracting geological and paleoenvironmental information. However, unmixing magnetic signals from complex magnetite and hematite mixtures is difficult because of the weak magnetization and high coercivity of hematite. We assess here the relative effectiveness of first-order reversal curve (FORC) and extended FORC-type diagrams, FORC-principal component analysis (PCA), isothermal remanent magnetization (IRM) curve decomposition, and PCA of remanent hysteretic curves for unmixing magnetic components in samples from the magnetically complex Inuyama red chert, Japan. We also further characterize the domain state and coercivity distributions of both magnetite and hematite with FORC-PCA and IRM acquisition analysis in the red chert. We show that IRM curve decomposition can provide valuable component-specific information linked to coercivity, while FORC-PCA enables effective magnetic domain state identification. PCA of remanent hysteretic curves provides useful information about the most significant factors influencing remanence variations and subtle coercivity changes. To identify components in complex magnetite and hematite mixtures, we recommend PCA analysis of remanent hysteretic curves combined with FORC analysis of representative samples to identify domain states and coercivity distributions.

1. Introduction

Paleomagnetic and environmental magnetic investigations typically involve analysis of geological samples that contain complex mixtures with different particle size components of the same magnetic mineral, or mixtures of magnetic minerals and particle size distributions. For example, pelagic marine carbonates, despite their often nearly pure white color, are generally magnetically complex and tend to contain mixtures of four components (Roberts et al., 2013): detrital magnetite, biogenic soft and hard (cf., Egli, 2004) magnetite, and detrital hematite. Terrigenous sediments also often contain complex magnetic mineral mixtures (e.g., Egli, 2004).

Comprehensive understanding of the magnetic signals recorded by natural samples requires use of suitable tools for quantitative identification of the contribution of each magnetic component. In environmental magnetic studies, it is valuable to understand such contributions because magnetic mineral components within mixtures can have multiple origins and/or represent multiple environmental processes. Unmixing helps to extract information on specific environmental and climate processes and sometimes unlocks quantitative interpretation of the respective magnetic components (e.g., Channell et al., 2016; Deng et al., 2006; Heslop & Roberts, 2012; Hunt et al., 1995; Larrasoaña et al., 2003; Maxbauer et al., 2017; Roberts et al., 2018). In paleomagnetic studies, quantitative evaluation of the contribution of different magnetic components is undertaken less frequently, but it can be important. For example, regionally or globally coherent relative paleointensity (RPI) signals can be recorded by sediments (e.g., Channell et al., 2009; Valet et al., 2005; Yamazaki & Oda, 2005; Ziegler et al., 2011), although the co-occurrence of biogenic and detrital magnetite with different recording efficiencies can complicate RPI signal recording (Chen et al., 2017; Ouyang

et al., 2014; Roberts et al., 2012). Thus, magnetic mineral unmixing is important for both paleomagnetism and environmental magnetism.

Many techniques have been developed to enable magnetic mineral unmixing. Paleomagnetic studies often exploit Curie temperature or thermal demagnetization of isothermal remanent magnetization (IRM) (Ando et al., 2001; Jiang et al., 2017; Lowrie, 1990; Oda & Suzuki, 2000). Other approaches make use of IRM curve analysis (e.g., Egli, 2003; Heslop & Dillon, 2007; Heslop et al., 2002; Kruiver et al., 2001; Maxbauer et al., 2016; Robertson & France, 1994; Zhao et al., 2018), alternating field (AF) demagnetization characteristics of isothermal and anhysteretic remanent magnetizations (ARMs) (Egli, 2004; Lagroix & Guyodo, 2017; Liu et al., 2002), a combination of hysteresis and ARM parameters (Lascu et al., 2010), and hysteresis loop unmixing (Heslop & Roberts, 2012). First-order reversal curve (FORC) unmixing has become possible (Lascu et al., 2015), and the improved algorithm of Harrison et al. (2018) enables solution of the linear mixing equation that facilitates identification and quantification of linearly additive magnetic components.

Hematite often carries important environmental information (Abrajevitch et al., 2014, 2018; Jiang et al., 2017), and separating hematite signals from those of ferrimagnetic minerals can be crucial for interpreting environmental change (Abrajevitch et al., 2013). Quantifying contributions from hematite within artificial magnetite/hematite mixtures is challenging. Hejda et al. (1994) found that the overall hysteresis loops for magnetite and hematite mixtures do not represent a simple sum of contributions corresponding to individual components. Muxworthy et al. (2005) measured FORC diagrams for artificial magnetite/hematite mixtures and found critical concentrations at which the magnetite signal swamped the hematite signal, rendering the hematite undetectable. They found that when hematite was less than ~81% of the mixture by mass, it was barely detectable using FORC diagrams. Similarly, by combining numerical micromagnetic simulations and FORC measurements for magnetite/hematite mixtures, Carvallo et al. (2006) found that hematite must comprise >88% of a mixture by mass to be detectable. Frank and Nowaczyk (2008) undertook magnetic measurements on magnetite/hematite mixtures and concluded that the contribution of hematite to the magnetic fraction must exceed 95 wt-% to visibly influence commonly used magnetic grain size and coercivity parameters. Ahmadzadeh et al. (2018) concluded that it is challenging to identify hematite using hysteresis loops, FORCs, or thermal demagnetization when magnetite contributes more than 5 wt-% to the mixture. Ahmadzadeh et al. (2018) suggested that IRM demagnetization curves are the most effective technique to quantify hematite in mixtures. Liu et al. (2019) studied mixtures of single domain magnetite and hematite with a broad grain size distribution and demonstrated that for hysteresis parameters and FORC measurements, hematite must be present in high concentrations (>90 wt-%) to be detectable, while at least 30 wt-% hematite is needed to be detectable in IRM or backfield IRM curves.

Magnetite–hematite mixtures pose a stringent test of the limitations of unmixing methods, which is why we seek here to test the effectiveness of different magnetic unmixing approaches for natural magnetite–hematite mixtures. We also assess the potential to combine unmixing methods because any approach that can improve diagnosis of magnetite–hematite mixtures should become widely useful for magnetic unmixing of geological samples.

Rhythmically bedded cherts provide a record of pelagic deep-sea environments from the Ordovician to the early Late Cretaceous (Jones & Murchey, 1986). The presence of datable microfossils and a paleohorizontal reference provided by well-developed bedding surfaces makes bedded chert sequences indispensable for reconstructing the tectonic histories of Paleozoic and early Mesozoic oceans. Mössbauer spectroscopy of Permian to Triassic Japanese cherts has revealed the presence of hematite, pyrite, and goethite, with hematite being the main iron-containing mineral (Matsuo et al., 2002). If it is only present in low concentrations, magnetite can be difficult to detect using Mössbauer spectroscopy. In contrast, magnetite can be detected readily even at low concentrations with magnetic techniques. Previous paleomagnetic studies of the Inuyama red cherts revealed both hematite and magnetite as the main natural remanent magnetization carriers (Ando et al., 2001; Oda & Suzuki, 2000; Shibuya & Sasajima, 1986) based on their unblocking temperatures. Electron probe microanalysis of representative microspherules in red cherts indicates that magnetite is present, with compositions similar to those in cosmic microspherules from other regions and to magnetite grains in carbonaceous chondrites (Iwahashi et al., 1991). Based on detailed rock magnetic characterizations, including IRM unmixing, Abrajevitch et al. (2011, 2013) inferred the presence of detrital and biogenic magnetite and pigmentary hematite. The complex mixture of magnetite and hematite in red cherts provides

an opportunity to assess the effectiveness of magnetic unmixing methods. In this study, we use FORC diagrams, IRM acquisition curve decomposition, FORC-principal component analysis (PCA) unmixing, and PCA of remanent hysteretic curves to reveal magnetic mineral assemblages in red chert samples from Inuyama, Japan. At the same time, we assess the effectiveness of these advanced techniques for characterizing complex mixtures of magnetite and hematite.

2. Materials and Methods

The studied rocks consist of rhythmically interbedded cherts (1–10 cm in thickness) and shales (1–3 mm in thickness) that accumulated at equatorial latitudes in the Panthalassa Ocean (Ando et al., 2001). The studied sequence contains a Triassic–Jurassic boundary (Figure S1b), which was accreted onto the Asian margin during the Jurassic and is exposed as a highly deformed but coherent thrust sheet in the Inuyama area, about 30 km north of Nagoya, Japan. The red chert samples used in this study are from the study of Oda and Suzuki (2000). Alternations of cherts and clastic rocks in the field are regarded to represent a pile of stacked thrust sheets that were emplaced during Jurassic accretion (Kimura & Hori, 1993). Beside these lithological repetitions, the stacked thrust sheets have been folded in the Sakahogi Synform to produce westward plunging fold axes (Kondo & Adachi, 1975). The Inuyama red chert is composed mainly of cryptocrystalline quartz with minor Fe-bearing minerals, such as illite, chlorite, smectite, hematite, and magnetite (Nakada et al., 2014). Red cherts were sampled at nine sites along Kiso River (Figure S1a); six at the Katsuyama (KA1–KA6, 35°25′21″N, 136°58′16″E), two at the Unuma (UN1, UN2, 35°23′54″N, 136°57′33″E), and one at the Momotaro (MO1, 35°24′16″N, 136°57′48″E) sections, respectively. At each site, 2–10 samples were chosen from those taken by Oda and Suzuki (2000) from a single chert bed forming a mesoscopic fold (several meters of wavelength) and cut into fresh rectangular samples with 4 × 4 × 2 mm dimensions. We analyzed 48 red chert samples in total.

All samples were measured with an alternating gradient magnetometer (Micromag 2900 AGM; Princeton Measurements Corporation) at the National Institute of Advanced Industrial Science and Technology, Tsukuba, Japan. Magnetic hysteresis loops were measured up to 1.4 T at 2.5 mT field steps with a 100 ms averaging time. For weakly magnetized samples, hysteresis loops were measured 3–5 times and averaged. We measured 120 FORCs per sample up to 1.4 T for all 48 samples using the irregular grid measurement protocol of Zhao et al. (2015). An irregular grid was used for FORC measurements because it allows measurement to 1.4 T while maintaining high-measurement resolution in the low-coercivity range. Importantly, the irregular grid protocol also reduces measurement time, thus diminishing the detrimental effects of measurement drift. Along with conventional FORC measurements (Pike et al., 1999; Roberts et al., 2000), we measured remanent FORC (remFORC) data, which allowed calculation of transient FORC (tFORC), and induced (iFORC) distributions to provide additional valuable information for domain state and magnetic mineral identification (Hu et al., 2018; Roberts et al., 2019; Zhao et al., 2017).

Conventional FORC datasets were imported into FORCinel (Harrison & Feinberg, 2008) and were processed with the VARIFORC smoothing algorithm (Egli, 2013), with resampling on a 2-mT grid. PCA was used to select end-members with the algorithm of Harrison et al. (2018) that employs combined feasibility metrics to ensure saturation and monotonicity and to avoid solutions in which FORCs cross each other.

Red chert samples are weakly magnetic, and the remanent magnetization is difficult to measure for small samples on an AGM. Although a long averaging time (5 s) was used, IRM acquisition curves were still too noisy for high-resolution decomposition analyses. The measured hysteresis loops were slope-corrected, normalized, and fitted with HystLab (Paterson et al., 2018). Under the assumption that hysteresis loops for geological materials exhibit inversion symmetry (Jackson & Solheid, 2010), the upper $M^{+}(B)$ and lower $M^{-}(B)$ branches of a slope-corrected and normalized loop can be used to estimate the induced hysteretic, M_{ih} and remanent hysteretic, M_{rh} curves (Rivas et al., 1981), which can be considered as backfield demagnetization curves. We calculated both M_{ih} and M_{rh} curves from fitted hysteresis loops. The S ratio was also calculated using the M_{rh} curve, where $S_{-300} = (1 - \mathrm{IRM}_{-300\,mT}/\mathrm{IRM}_{1.4T})/2$ and $S_{-100} = (1 - \mathrm{IRM}_{-100\,mT}/\mathrm{IRM}_{1.4T})/2$ (Bloemendal et al., 1992). PCA was carried out on the M_{rh} curves, which were transformed to represent IRM acquisition and then unmixed using the MAX Unmix software (Maxbauer et al., 2016), which employs a skewed-normal distribution (Wuertz & Chalabi, 2015) to represent individual coercivity components.

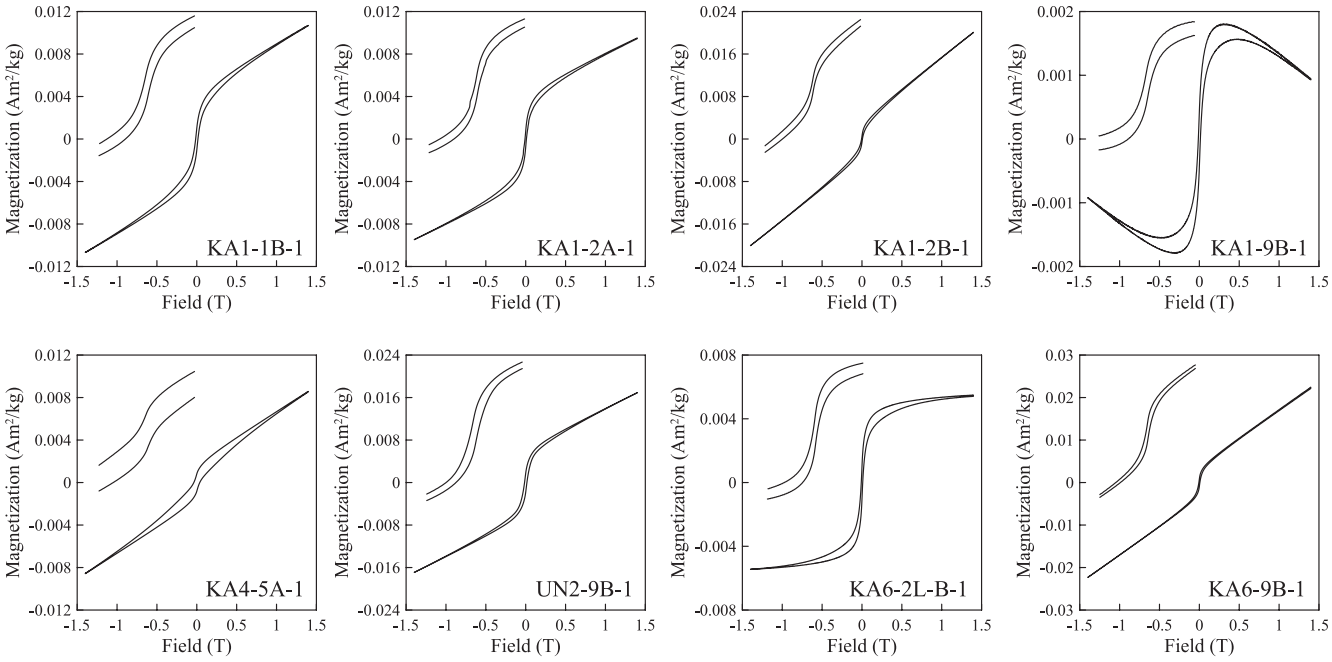

Figure 1. Measured hysteresis loops (without high-field slope correction) for selected red chert samples (maximum applied field is 1. 4 T). The inset in each figure is for the expanded low field range from −200 to 200 mT to demonstrate the wasp-waisted form of the hysteresis loops.

3. Hysteresis Loops and Irregular FORCs

Hysteresis loops for selected red chert samples are illustrated in Figure 1. Variable loop shapes are observed, such as narrow loops for samples KA1-2B-1 and KA6-9B-1, an S-shaped loop for sample KA1-9B-1, and constricted loops for samples KA6-2L-B-1, KA1-1B-1, and KA1-2A-1. The loop shapes indicate diverse paramagnetic, most likely clay minerals, and diamagnetic (quartz) contributions to the red chert samples. None of the measured loops close until fields >700 mT or higher. Based on previous red chert studies, this is most likely due to hematite. Moreover, loops are clearly wasp-waisted (Figure 1). The hysteresis shape parameter, σ, calculated following Fabian (2003) using HystLab (Paterson et al., 2018), is a quantitative indicator of wasp-waisted or potbellied loops, with $\sigma > 0$ for wasp-waisted loops and <0 for potbellied loops. The logarithmic definition of σ is intended to obtain a measure of shape variation from potbellied to wasp-waisted loops (Fabian, 2003). Red chert samples have high positive σ values (0.97–2.65), which are indicative of strongly wasp-waisted behavior. Wasp-waisted loops result from subpopulations of magnetic grains with widely different coercivities, which can arise from mixtures of grain sizes of a single magnetic mineral or from a combination of magnetic minerals with markedly different coercivities (Roberts et al., 1995; Tauxe et al., 1996). Here, the significant contribution from hematite, mixed with magnetite, explains the wasp-waisted loops. However, mixtures of grain sizes of magnetite or/and hematite could also contribute to the wasp-waisted behavior.

Conventional FORC, remFORC, iFORC, and tFORC diagrams are shown in Figures 2 and 3 for four representative red chert samples. Most Triassic red chert samples have similar FORC distributions to sample KA1-1B-1 (Figures 2a–2d), which has dominantly stable single domain (SD) behavior, as indicated by the "negative–positive–negative" iFORC pattern (Figure 2c) (Hu et al., 2018; Zhao et al., 2017) and a significant hematite contribution with coercivity up to 1.2 T in conventional and remFORC diagrams (Figures 2a and 2b). The low-coercivity component has a positive peak at $B_c \approx 10$ mT (Figure S2). Signals due to particles with viscous magnetizations near the superparamagnetic (SP) to stable SD threshold size are also present in the remFORC diagram, as indicated by a positive region along the $B_i < 0$ axis (Figure 2b). The presence of vortex state particles is confirmed by the tFORC diagram, which has two positive lobes along the B_i axis (Hu et al., 2018; Zhao et al., 2017).

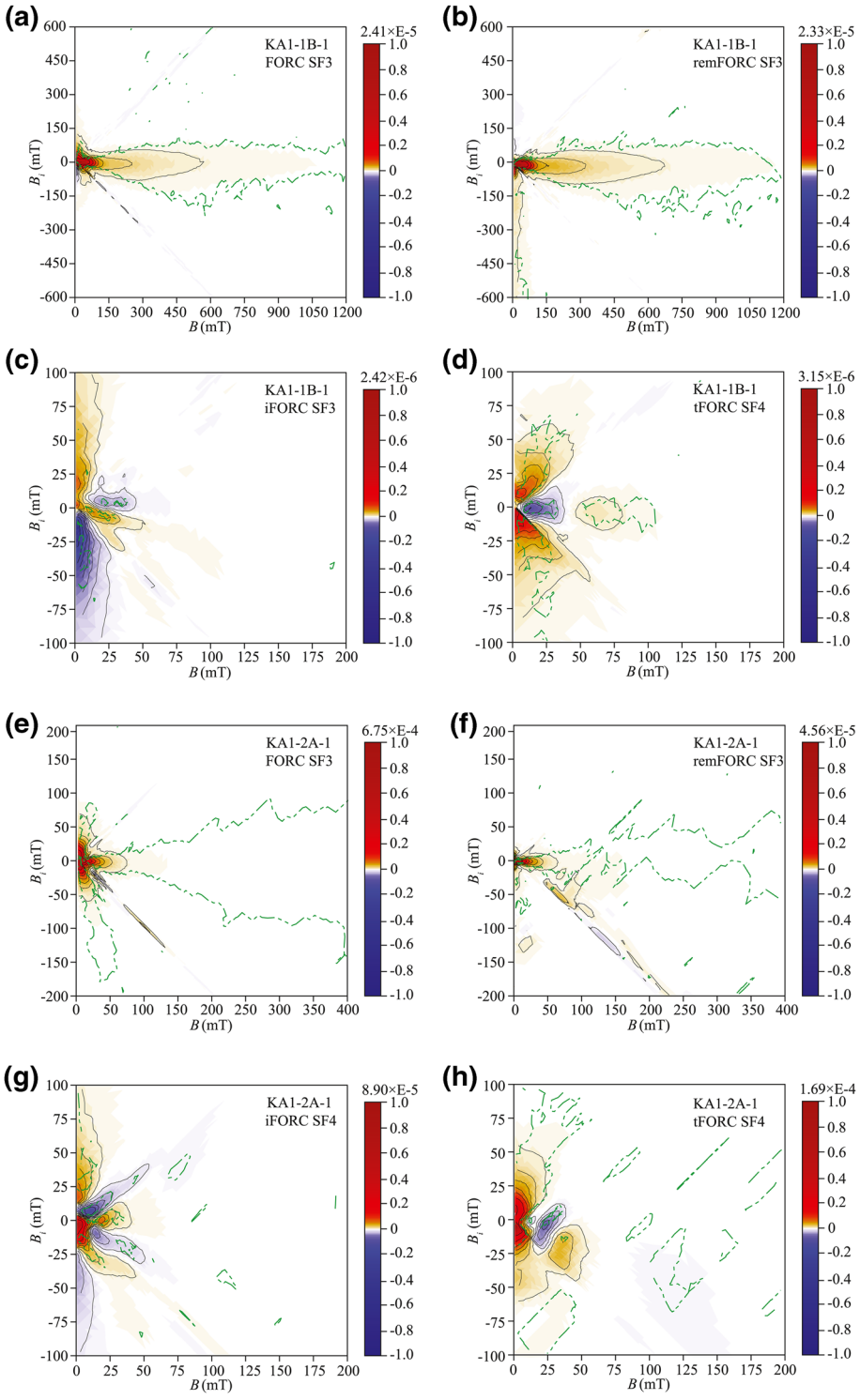

Figure 2. (a), (e) Conventional FORC, (b), (f) remFORC, (c), (g) iFORC, and (d), (h) tFORC diagrams for Triassic red chert samples KA1-1B-1 and KA1-2A-1. Dashed green lines represent the 0.05 significance level calculated following Heslop and Roberts (2012).

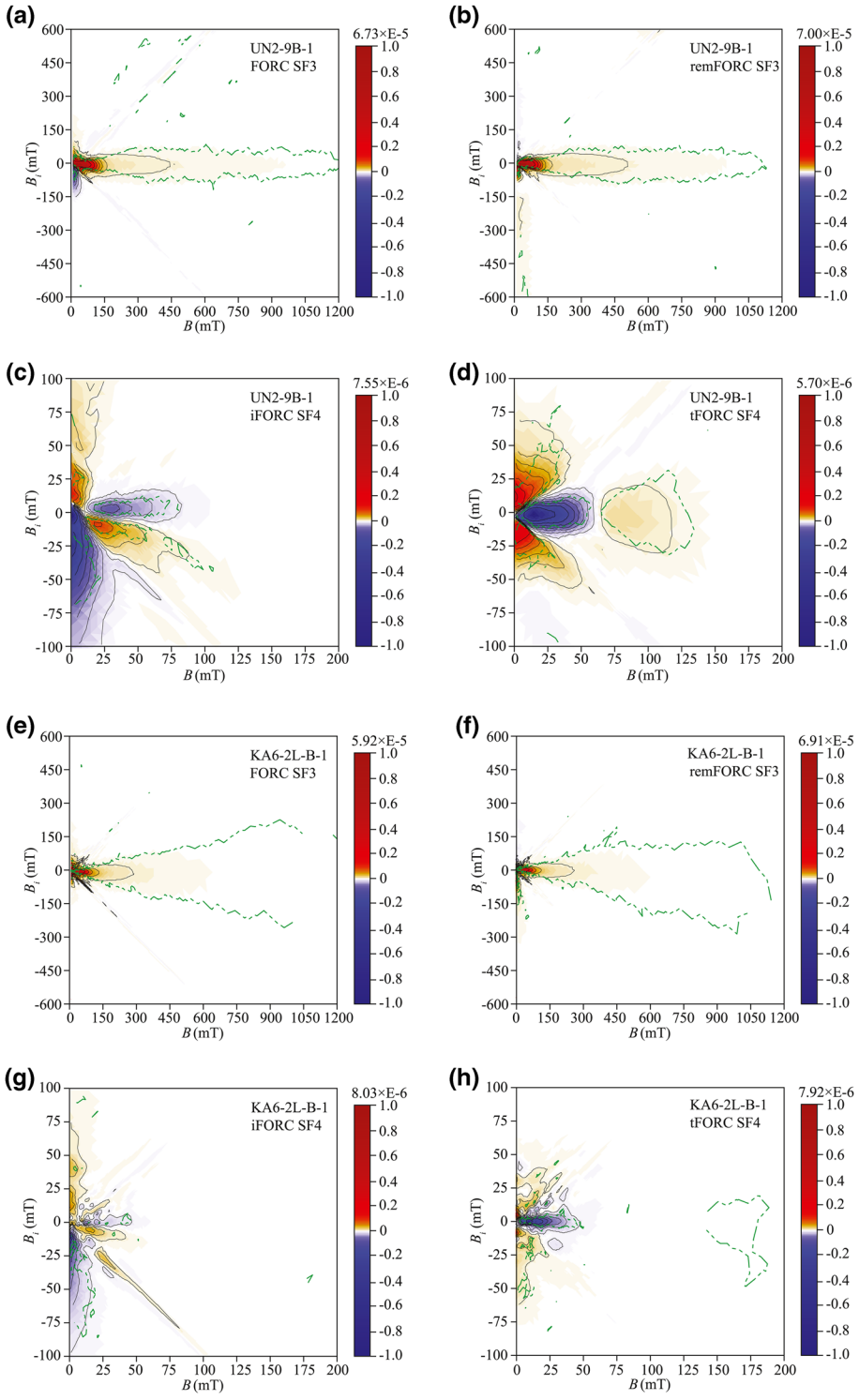

Figure 3. (a), (e) Conventional FORC, (b), (f) remFORC, (c), (g) iFORC, and (d), (h) tFORC diagrams for upper Triassic red chert sample UN2-9B-1 and lower Jurassic red chert sample KA6-2L-B-1. Dashed green lines represent the 0.05 significance level calculated following Heslop and Roberts (2012).

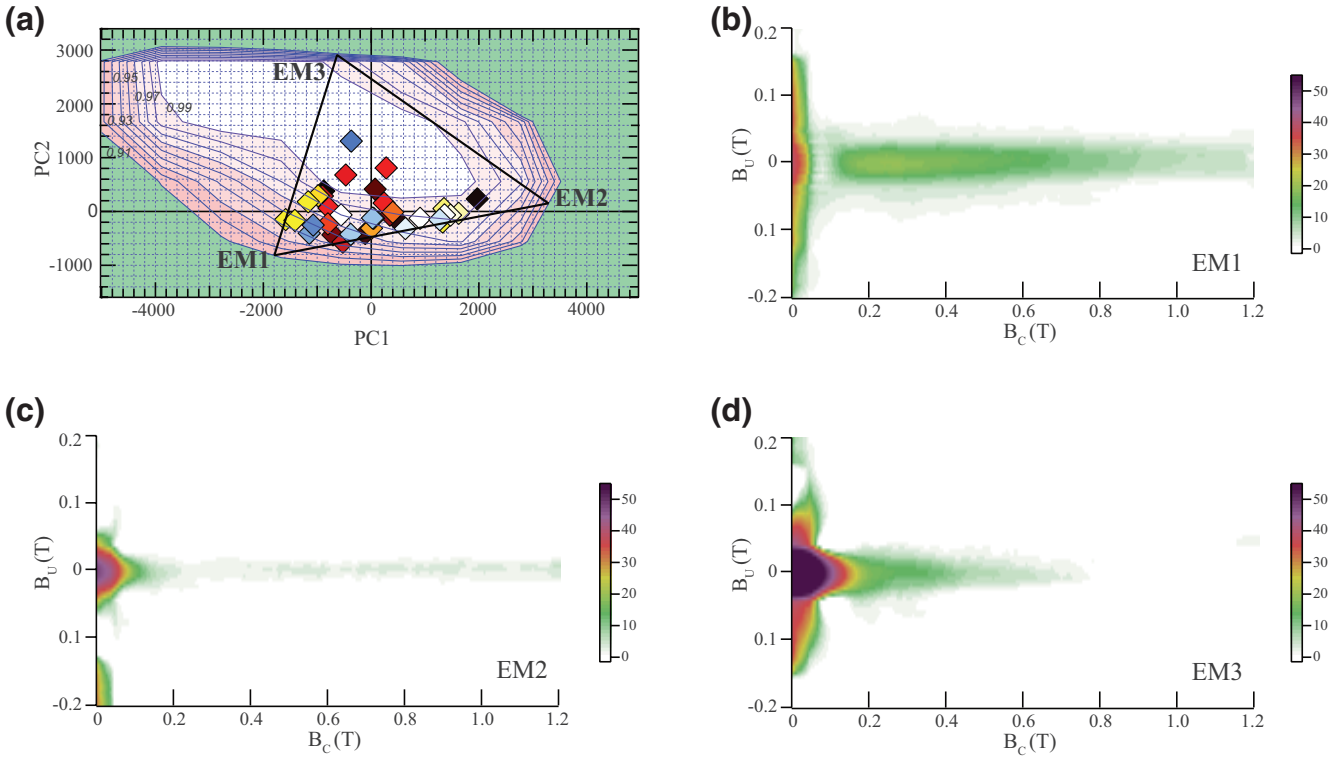

Figure 4. FORC-PCA results for the whole applied field range (0–1.2 T) for Inuyama red chert samples. FORCs were mass normalized and smoothed using VARIFORC parameters; $S_{c0} = 4$, $S_{c1} = 4$, $S_{b0} = 4$, $S_{b1} = 4$, $\lambda_c = 0.3$, and $\lambda_b = 0.3$. (a) PC score plots for a ternary mixing space between EM1, EM2, and EM3. Diamonds represent the scores of individual samples. Contour lines represent the combined feasibility metric for the saturation, monotonicity, and crossing metrics. (b)–(d) Reconstructed FORC diagrams for EM1, EM2, and EM3, respectively, derived from the whole measured applied field range.

Only a few Triassic samples have FORC diagrams similar to that of KA1-2A-1, which is a dominant vortex state signal illustrated by the "negative–positive–negative–positive" pattern in the iFORC diagram (Figure 2g). Hematite makes a weak contribution to the magnetization of this sample, which also contains particles near the SP/SD threshold size (Figure 2f). Noninteracting SD behavior with a central ridge signature starts to dominate in upper Triassic sample UN2-9B-1 and Jurassic sample KA6-2L-B-1, together with a hematite contribution (Figures 3a, 3b, 3e, and 3f). For UN2-9B-1, viscous SP/SD and vortex state signals are also present in the remFORC and tFORC diagrams, respectively (Figures 3b and 3d), while KA6-2L-B-1 is dominated by SD features (Figure 3g). The low-coercivity components for both samples also have peaks at $B_c \approx 10$ mT (Figure S2).

4. FORC-PCA

Data for 37 samples were analyzed using FORC-PCA; 11 datasets, mainly for weakly magnetized samples were excluded due to noisy data with large measurement drift. Initial FORC-PCA was performed for the 0–1.2 T field range (Figures 4a–4d), followed by FORC-PCA for the range 0–0.12 T (Figures 5a–5d). A triangular region in the PC1–PC2 plane defines a three end-member (EM) system, where FORC diagrams for the three EMs are shown in Figures 4b–4d. The triangle that defines the three EM mixing system falls within a broader zone enclosed by shaded feasibility contours, which define an area with physically meaningful FORC diagrams (Harrison et al., 2018). To capture the high-coercivity hematite signal, a relatively large VARIFORC λ value is used for smoothing, which may lead to distortion in the low-coercivity range of the FORC diagram. Therefore, we discuss details of low-coercivity features in Figure 5.

EM1 contains a high-coercivity ridge and a low-coercivity multidomain (MD) component (Figure 4b). Given that the ferrimagnetic signal is expected to dominate at lower coercivities and hematite would need to be

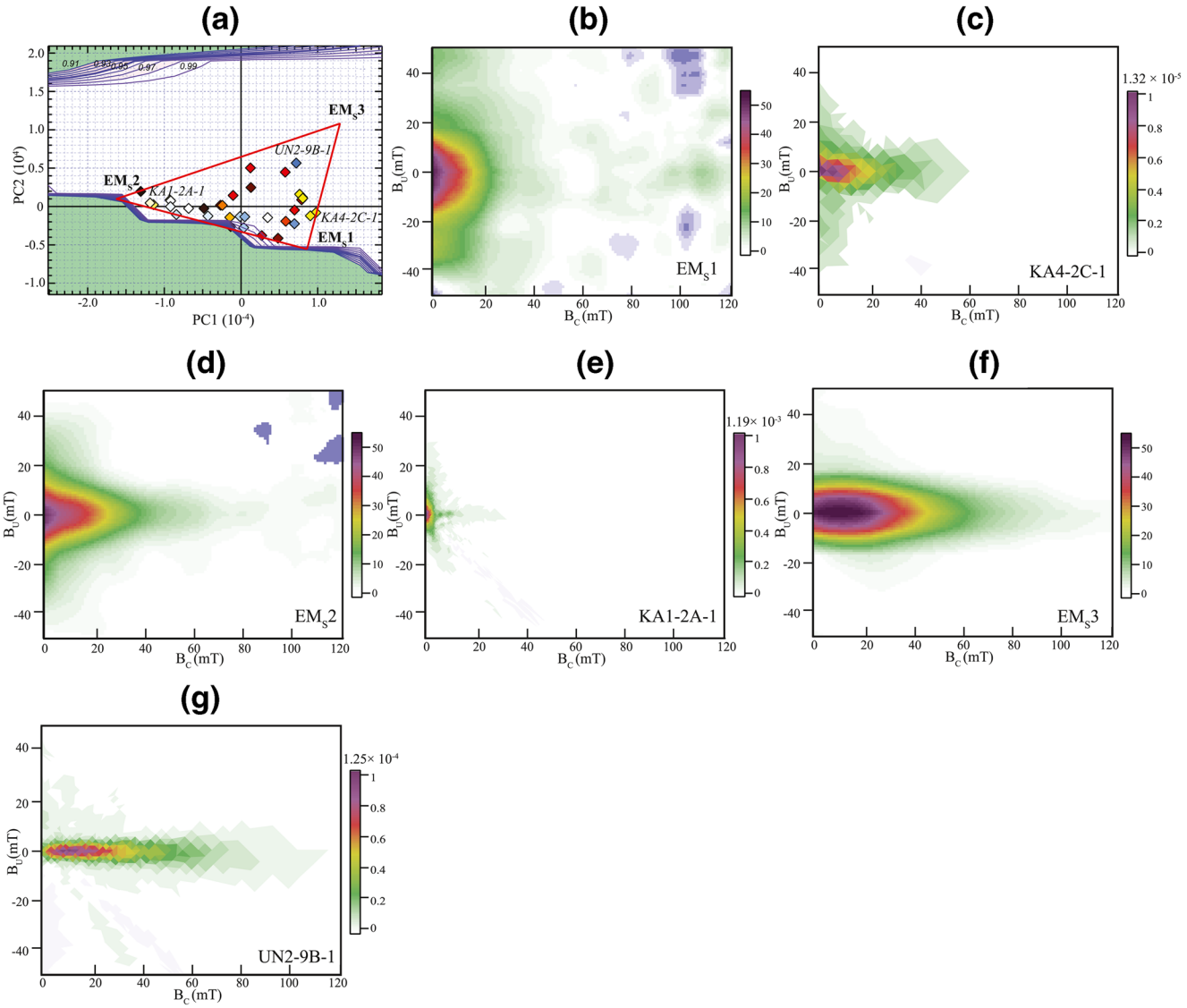

Figure 5. FORC-PCA results for the 0–0.12 T applied field range for Inuyama red chert samples. (a) PC score plots for a ternary mixing space between EM_S1, EM_S2, and EM_S3. Diamonds represent the scores of individual samples. Contours represent the combined feasibility metric for the saturation, monotonicity, and crossing metrics. (b, d, f) Reconstructed FORC diagrams for EM_S1, EM_S2, and EM_S3, respectively, from the low coercivity applied field range compared with FORC diagrams for samples (c) KA4-2C-1, (e) KA1-2A-1, and (g) UN2-9B-1. FORCs were mass normalized and smoothed using $S_{c0} = 2$, $S_{c1} = 2$, $S_{b0} = 2$, $S_{b1} = 2$, $\lambda_c = \lambda_b = 0$ for FORC-PCA and a smoothing factor of two for high-resolution FORCs.

larger than ~100 μm to have a coercivity of ~10 mT (Özdemir & Dunlop, 2014), this MD component is likely to be MD magnetite/maghemite. EM2 contains low-coercivity SD particles and a smaller high-coercivity contribution (Figure 4c). EM3 has SD features, a vortex state component that spreads across the B_u axis and an apparently weaker hematite contribution (Figure 4d).

S ratios are also employed as a means to quantify the relative hematite contribution to each end-member identified in the FORC-PCA. The *S* ratios of red chert samples range from 0.40 to 0.85 for S_{-300} and 0.23 to 0.74 for S_{-100}. A negative relationship is observed between the EM1 contribution and both S_{-300} and S_{-100} (Figures 6a and 6d) and negative and low *S* ratios occur as EM1 becomes dominant (Figures 6b and 6c). This is because EM1 represents a high-coercivity hematite contribution. EM3 is dominantly a low-coercivity component, which has a positive relationship with the *S*-ratio values (Figures 6c and 6f). The observation that S_{-100} correlates linearly with EM3, in addition to S_{-300}, suggests that hematite also

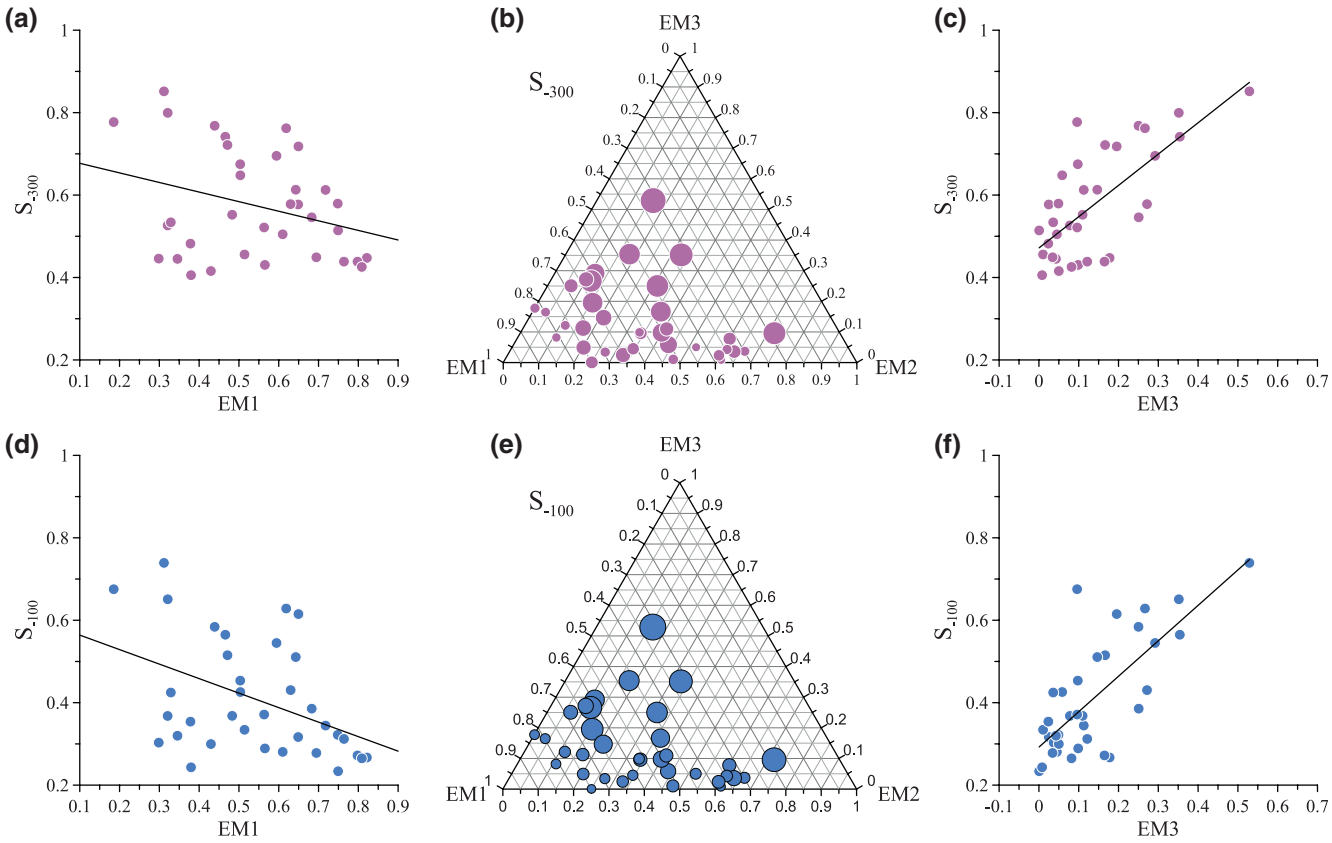

Figure 6. *S*-ratio variations with respect to different FORC-PCA EMs, with a weak negative relationship between EM1 and (a) S_{-300} and (d) S_{-100}; ternary diagram of (b) S_{-300} and (e) S_{-100} variations with respect to the 3 EMs, where the size of the circles represents S_{-300} values ranging from 0.40 to 0.85 and S_{-100} ranging from 0.23 to 0.74, respectively; and increasing (c) S_{-300} and (f) S_{-100} with increasing EM3 contributions.

exists in the lower coercivity component (i.e., 100–300 mT), which is confirmed by PCA analysis of M_{rh} curves presented below.

FORC-PCA was performed for the low field range from 0 to 120 mT to determine the domain state of the ferrimagnetic mineral fraction (Figures 5a–5d). Three EMs are identified, which we refer to as EM_S1, EM_S2, and EM_S3, respectively. The high-resolution FORC diagrams of samples close to each EM are also provided in Figure 6. EM_S1 has low B_c with vertical spreading along the B_u axis (Figure 5b), which corresponds to the MD feature of EM1. The high-resolution FORC of KA4-2C-1 shows mixed features of coarse and SD particles (Figure 5c). When moving toward EM_S1, the SD signal gradually decreases and the MD features remain as EM_S1. EM_S2 represents a vortex feature which is also confirmed by the high-resolution FORC of KA1-2A-1 (Figure 5e). EM_S3 has a noninteracting SD central ridge with maximum at 15 mT (Figure 5f), which is shown more clearly in the high-resolution FORC of UN2-9B-1 (Figure 5g). Abrajevitch et al. (2011, 2013) interpreted the FORC central ridge signature to represent biogenic magnetite in the Inuyama red chert.

5. Remanent Hysteretic Curve PCA

Hysteresis loops were processed using HystLab (Paterson et al., 2018) for loop centering and drift correction, and were fitted following similar procedures to Von Dobeneck (1996) and Jackson and Solheid (2010). The fitted magnetizations were normalized by their maximum values. The symmetry of hysteresis loops implies that there exist correspondingly symmetric curves M_{rh} and M_{ih}, the remanent hysteretic and induced hysteretic magnetizations (Jackson & Solheid, 2010), which are calculated as $M_{rh}(H) = (M^+(H) - M^-(H))/2$ and $M_{ih}(H) = (M^+(H) + M^-(H))/2$, respectively, where $M^+(H)$ and $M^-(H)$ are the upper and lower hysteresis loop branches. Paramagnetic and diamagnetic contributions to hysteresis loops are typically

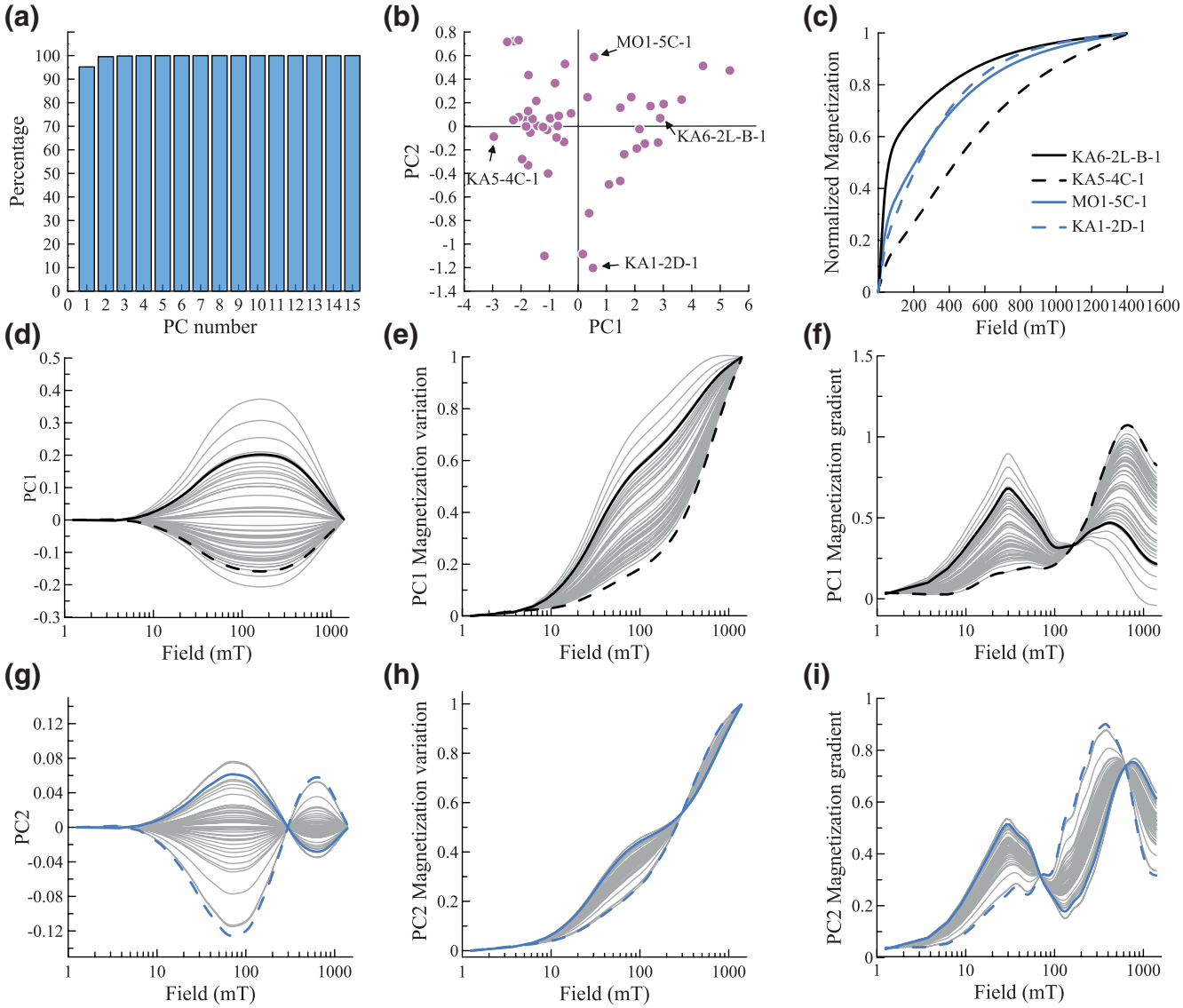

Figure 7. PCA results for M_{rh} curves. (a) Percentage of total variance represented by different numbers of PCs; (b) biplots of PC1 and PC2 scores; (c) four representative reconstructed IRM acquisition curves for samples with the maximum (black solid line) and minimum (black dashed line) PC1 scores along the PC2 axis and samples with the maximum (blue solid line) and minimum (blue dashed line) PC2 scores along the PC1 axis. (d, e, f) PC1 variation with applied field for M_{rh} curves, reconstructed normalized IRM acquisition curves for PC1, and corresponding gradient variation; PC2 was set to zero for each sample; (g, h, i) PC2 variation with applied field for M_{rh} curves, reconstructed normalized IRM acquisition curves for PC2, and corresponding gradient variation in log scale; PC1 was set to zero for each sample.

corrected by subtraction of a straight-line component estimated at high fields. In the presence of an unsaturated hematite component, however, such a correction is inappropriate. The significant hematite content in the red chert samples, thus, makes simple high-field slope correction infeasible. Therefore, PCA was performed solely on M_{rh} curves to avoid the slope correction issue and to reveal more detailed information concerning remanent magnetization variations. M_{rh} curves have even symmetry, so we performed PCA only on the positive field M_{rh} branch. PC loadings were calculated as a function of applied field (Figures 7d and 7g). Reconstructed M_{rh} curves were calculated for each PC (Figures 7e and 7h) and then transformed to represent IRM acquisition curves. We chose a model with two principal components, where PC1 accounts for ~95% of the variance (Figure 7a). Four representative samples along the PC1 and PC2 axes are chosen to illustrate variation of each PC (Figure 7b), with corresponding reconstructed IRM

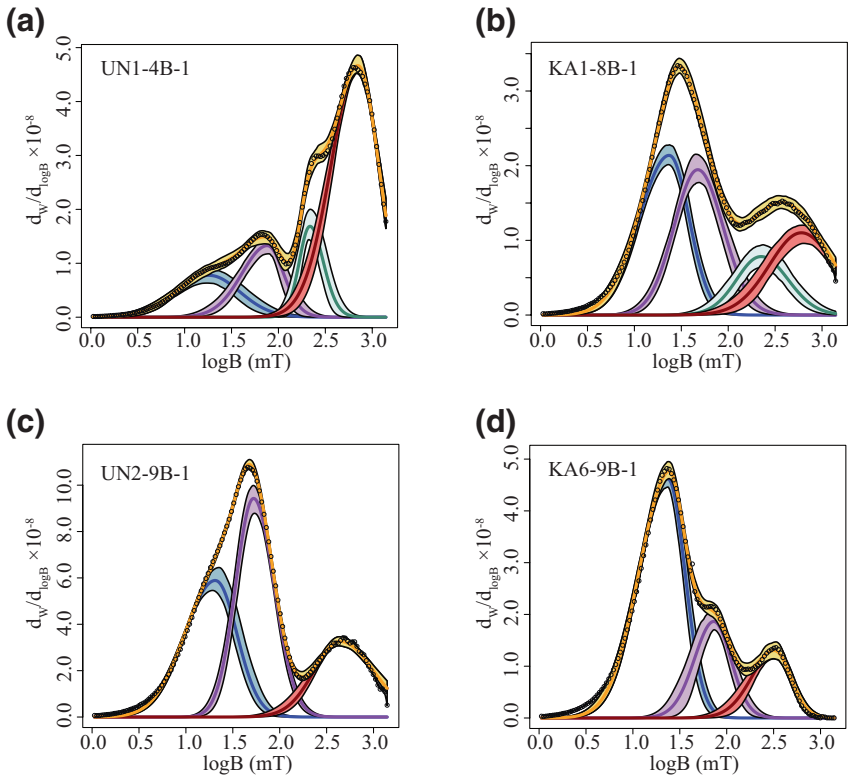

Figure 8. Example model fits for representative red chert samples. Coercivity distribution (gray circles are measured data). Shaded areas represent 95% confidence intervals. Blue, purple, green, and red lines represent fitted components 1, 2, 3, and 4, respectively. Yellow lines are the sum of the model components.

acquisition curves (Figure 7c). Sample KA6-2L-B-1, which has the highest PC1 score when PC2 ≈ 0, has a magnetite-dominated IRM acquisition curve. However, the IRM acquisition curve does not saturate even at 1.4 T, which indicates the presence of hematite. In contrast, sample KA5-4C-1, which has the lowest PC1 score, has a gradually increasing IRM acquisition curve until 1.4 T, which suggests a significant hematite contribution. For samples MO1-5C-1 and KA1-2D-1, which have the maximum and minimum PC2 scores in proximity to PC1 = 0, the biggest difference occurs at ~300 mT. Samples with higher PC2 scores have a larger contribution of a softer component (H_{cr} < ~300 mT) and a smaller contribution of a hard component (H_{cr} > 300 mT). Variation of each PC is illustrated in Figures 7d–7i. Variation along PC1 with magnetic field (PC2 fixed to zero), is shown in Figure 7d. Corresponding reconstructed IRM acquisition curves and their gradients are shown in Figures 7e and 7f, respectively. The same process was carried out for PC2 (Figures 7g–7i).

For PC1, magnetization varies for both low-coercivity (<~100 mT) and high-coercivity components (Figures 7e and 7f). Importantly, the low-coercivity and high-coercivity components do not have fixed coercivity distributions (Figure 8f); rather, they vary for both components among samples. The relative contributions of low-coercivity and high-coercivity components are shown by PC1, as illustrated by solid and dashed lines for samples with high-PC1 and low-PC1 scores, respectively (Figure 7f). For PC2, two peaks with opposite variations are present (Figure 7g). Coercivity distribution variations are observed in reconstructed IRM acquisition curves and their gradient (Figures 7h and 7i). For samples with low-PC2 scores (blue dashed line), the soft component peak shifts to higher values while the coercivity peak for the hard component shifts to lower values, which results in a larger intermediate coercivity contribution (~100 mT < B_{cr} < ~300 mT) (Figure 7i) and vice versa (Figure 7i). These changes are clearly evidenced as two trends in reconstructed IRM acquisition curves (Figure 7h).

Based on the above observations, PC1 for the M_{rh} curves represents relative variations between low-coercivity and high-coercivity components, which explains most (~95%) of the data variability. PC2 variations

reflect subtle coercivity shifts of the low-coercivity component and covariations between intermediate-coercivity (100–300 mT) and high-coercivity components, which suggest different mineral origins or transformation from one group to another (e.g., oxidation).

6. IRM Acquisition Curve Unmixing

IRM acquisition curve decomposition reveals the presence of 3–4 components (see Table S1 for all samples). When fitting these models, our strategy was to keep each component within a relatively constant coercivity range throughout the sample set. For example (Figure 8), IRM curves are fitted with three components for UN2-9B-1 and KA6-9B-1, while four components are needed for UN1-4B-1 (see Figure S3 for 2-component and 3-component fits). Each component is described by its characteristic median coercive field (B_h), dispersion parameter (DP; one standard deviation in $\log_{10}$ space), and skewness. Four typical types of fits are obtained (Figure 8). A low-coercivity component (C1) has B_h of 14–34 mT and DP of 0.23–0.34. Mean B_h for another low-coercivity component (C2) is higher than C1, and ranges from 42 to 90 mT with a smaller DP (0.14–0.28). C3 is an intermediate-coercivity component with B_h of 133–314 mT, and a wider DP (0.10–0.35). Lastly, a high-coercivity component (C4) has mean B_h of 357–1056 mT and DP of 0.21–0.38.

The coercivity of magnetite varies with domain state and particle size (Dunlop & Özdemir, 1997; Lee et al., 2015; Maher, 1988). Coercivity increases with grain size for SD magnetite, and then decreases with increasing MD size. Considering its low coercivity and large DP, C1 is interpreted to represent detrital magnetite, most likely in an MD or vortex state. C2 also represents a ferrimagnetic phase, with larger coercivity and narrow distribution, which suggests SD behavior.

From its coercivity, C3 can be interpreted to represent fine-grained hematite or oxidized magnetite, or a mixture of both. Its dispersion is generally <0.20; the relatively narrow coercivity distribution probably suggests a secondary origin for C3. C4 is interpreted as hematite due to its high coercivity up to 1 T. C4 is the main remanence carrier for most samples (Figure 8a), and accounts for ~50% or more of the total remanence. Samples from the oldest Anisian period (KA1, UN1; Figure S1b) have highly variable relative contributions of components; most samples have a lower C4 contribution (Figure 8b). Upper Triassic sample UN2-9B-1 has the largest contribution from C2 and less from C4. Magnetite is the dominant magnetic mineral for Jurassic sample KA6-9B-1, and no C4 is detected. However, this sample is red, which indicates that hematite also contributes to C3. This is consistent with the observation that hematite nanoparticles have low coercivity and bright red color (Cornell & Schwertmann, 2004, p. 664; Özdemir et al., 2014).

7. Discussion

7.1. Deciphering Complex Magnetic Mixtures Using Multiple Unmixing Techniques

By combining unmixing and PCA results, we provide new evidence concerning the magnetic domain state and interrelationship among coercivity components within the Inuyama red chert. The domain state of magnetic minerals is assessed directly by extended FORC-type diagrams and by FORC-PCA. Previous interpretations of FORC results focused on the noninteracting central ridge signal for magnetite (Abrajevitch et al., 2011, 2013). We used applied fields up to 1.2 T and irregular grid measurements, which also enables detection of hematite. Hematite is clearly evident as an extended positive signal along the B_c axis up to the maximum field in both FORC and remFORC diagrams (Figures 2a, 2b, 3e, and 3f). Most samples have dominantly SD behavior with a vortex state component, as evidenced by the negative–positive–negative feature in iFORC diagrams (Figures 2c, 3c, and 3g) and two positive lobes along the B_i axis of tFORC diagrams (Figures 2d and 3d) (Hu et al., 2018; Zhao et al., 2017). A few samples have dominant vortex state behavior that is evident as a negative–positive–negative–positive feature in iFORC diagrams (Figure 2g) (Hu et al., 2018; Zhao et al., 2017). Vertical distributions along the negative B_i axis in remFORC diagrams (Figures 2b and 3b) indicate that viscous SP/SD particles are widely present in red chert samples (Hu et al., 2018; Zhao et al., 2017).

FORC-PCA provides further domain state indications for EMs in red chert samples, which suggests a link among magnetic particles with different domain states. Hematite has SD behavior and appears to co-occur in EM1 with vortex state/MD ferrimagnetic minerals (Figure 4b), which likely represents a detrital input.

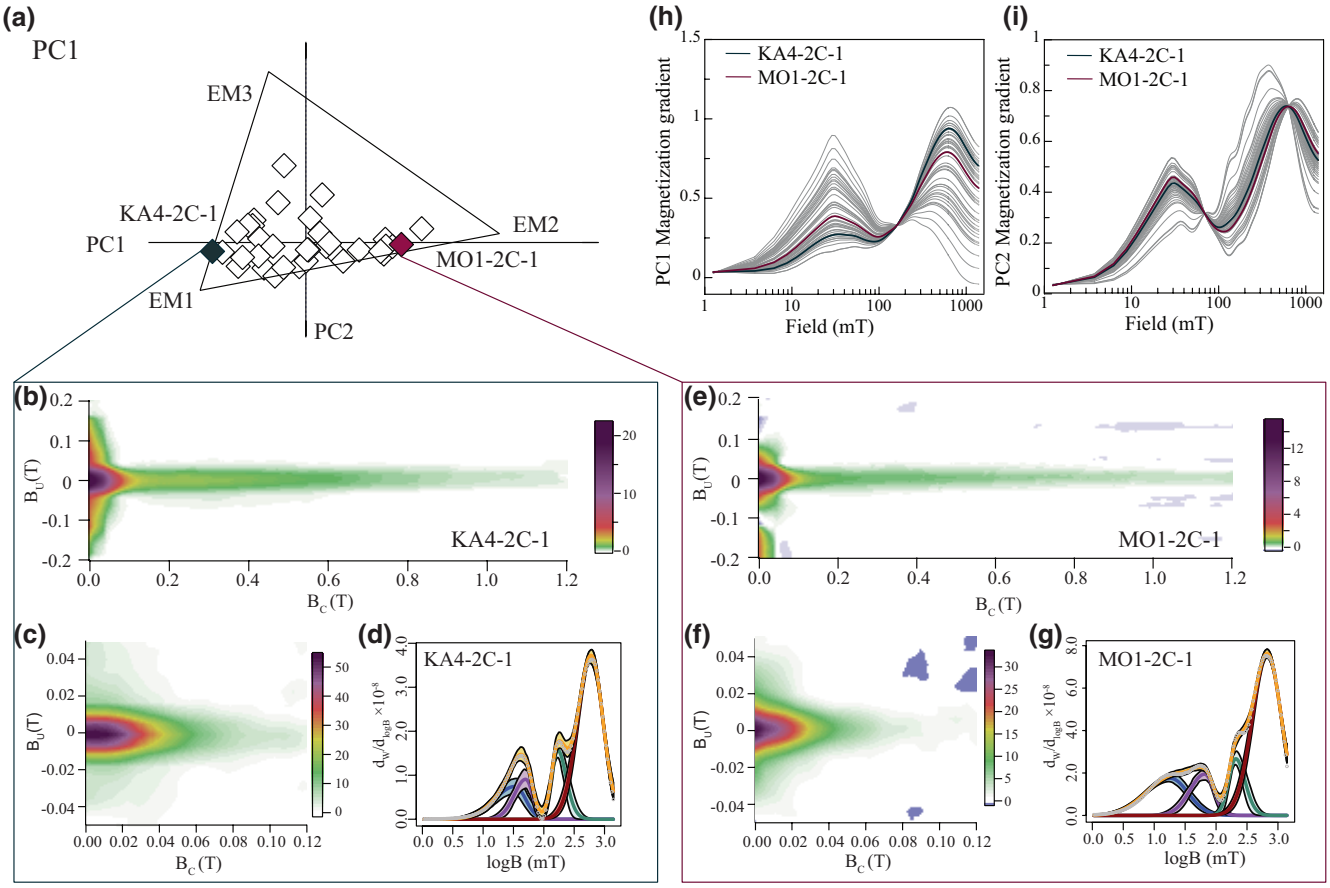

Figure 9. Comparison of FORC-PCA, IRM acquisition unmixing, and M_{rh} PCA results along the PC1 axis of the FORC-PCA solution. (a) PC space for the FORC-PCA solution; (b), (e) reconstructed FORC diagrams using two PCs for illustrated samples KA4-2C-1 and MO1-2C-1 for the full applied field range; and (c), (f) reconstructed FORC diagrams using the two PCs for samples KA4-2C-1 and MO1-2C-1 for the low field range from 0 to 120 mT. (d), (g) IRM acquisition unmixing results for samples KA4-2C-1 and MO1-2C-1. Blue, purple, green, and red lines represent components C1, C2, C3, and C4, respectively, and the yellow line represents the total magnetization. (h), (i) Magnetization gradients of PC1 and PC2 from PCA analysis of M_{rh} for all studied samples; blue and red lines represent results for samples KA4-2C-1 and MO1-2C-1, respectively.

As suggested by Abrajevitch et al. (2011), hematite contents in claystone layers are a few times higher than in adjacent chert layers, which points to a detrital hematite source. M_{rh} curve PCA reveals that magnetite and high-coercivity components (mainly hematite) explain most of the remanence variation. In addition, inverse variation of the 100–300 mT coercivity range and the high-coercivity component suggests that these two components have different origins or that the magnetite was oxidized to hematite.

7.2. Comparison of Unmixing Techniques

By comparing unmixing techniques and PCA results, the main magnetic property variation relates to coercivity, domain state, and the linked variation among coercivity components. Results of FORC-PCA, IRM acquisition unmixing, and PCA of M_{rh} curves are combined and illustrated in Figures 9 and 10. Extended FORC diagrams for these samples are shown in Figures S4 and S5 for reference. The PC space for FORC-PCA results for the whole field range from 0 to 1.2 T is shown in Figure 9a, along with reconstructed FORCs for samples that lie closest to the ends of the PC2 axes to illustrate PC1 variations across the sample set. Data for sample KA4-2C-1 lie on the left-hand end of the PC1 axis, where SD, vortex state, and hematite signals are evident in the FORC diagram for the entire applied field range (Figure 9b), while for the low field range the low-coercivity component is defined more reliably, with a dominant SD feature and a less significant vortex state background (Figure 9c). Four components are identified with IRM acquisition unmixing, where hematite makes the largest contribution to remanence (Figure 9d). For

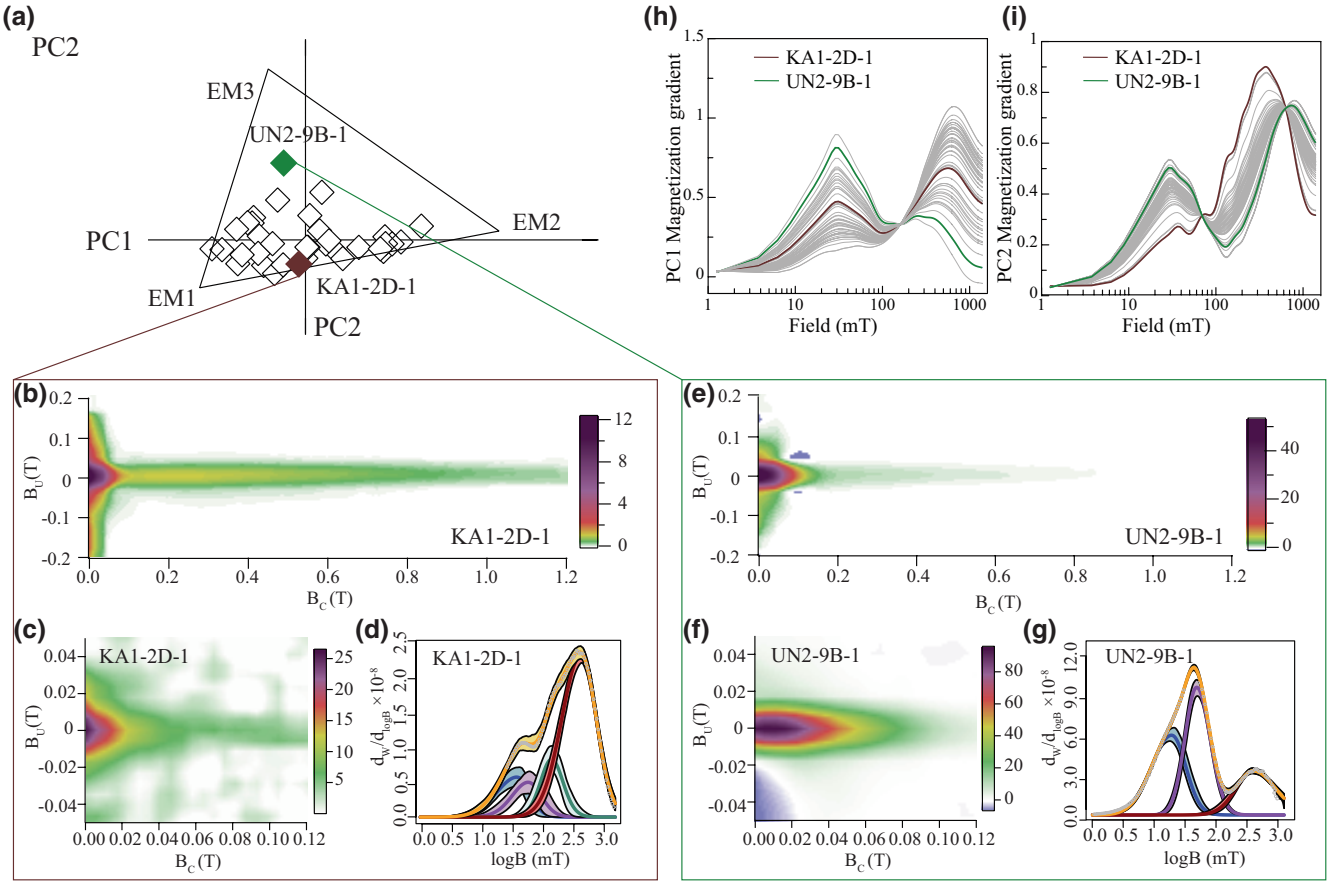

Figure 10. Comparison among FORC-PCA, IRM acquisition unmixing, and M_{rh} PCA results along the PC2 axis of the FORC-PCA solution. (a) PC space for the FORC-PCA solution; (b), (e) reconstructed FORC diagrams using two PCs for the whole applied field range for samples KA1-2D-1 and UN2-9B-1; (c), (f) reconstructed FORC diagrams using two PCs for samples KA1-2D-1 and UN2-9B-1 for the 0–120 mT range; and (d), (g) IRM acquisition unmixing results for samples KA1-2D-1 and UN2-9B-1. Blue, purple, green, and red lines represent components C1, C2, C3, and C4, respectively. The yellow line represents the total magnetization. (h), (i) Magnetization gradient of PC1 and PC2 from M_{rh} PCA; brown and green lines represent results for samples KA1-2D-1 and UN2-9B-1, respectively.

PC1 from M_{rh} curve PCA, hematite also makes a larger contribution than magnetite (Figure 9h). When moving from left to right on the FORC PC1 axis, data for sample MO1-2C-1 have more significant vortex behavior and a smaller SD signal (Figure 9f). Correspondingly, in IRM decomposition spectra, C1 has a larger contribution and a wider distribution at low coercivities (blue component, Figure 9g). In M_{rh} PCA results, MO1-2C-1 has larger soft components than KA4-2C-1 (Figure 9h). However, hematite is still present in sample MO1-2C-1 and its relative contribution does not change significantly (Figure 9h). Therefore, for FORC-PCA, PC1 mainly represents a domain state change in the low-coercivity components, from SD behavior to a more vortex state behavior, which suggests either a coarsening process or a decrease in SD ferrimagnetic mineral content.

Magnetic property changes along the FORC-PCA PC2 axis are shown in Figure 10. Data for sample KA1-2D-1 lie at the lower end of the PC2 axis and are dominated by hematite. Its ferrimagnetic component has lower coercivity (Figures 10b and 10c). When moving to the upper end of the PC2 axis, sample UN2-9B-1 has a strong noninteracting SD signal with a minor hematite contribution (Figures 10e and 10f). From M_{rh} curve PCA results, the largest difference between KA1-2D-1 and UN2-9B-1 is the relative contribution from high-coercivity and low-coercivity components (Figure 10h). Moreover, sample UN2-9B-1 also lacks the intermediate-coercivity component (100–300 mT), which is clear in PC2 of the M_{rh} curve PCA results (Figure 10i) and C3 is absent in IRM acquisition curve decomposition (Figure 10g). Therefore, PC2 of FORC-PCA mainly represents a change in the relative contribution of low and higher coercivity minerals, and a change in the intermediate-coercivity component.

The comparison above indicates that FORC-PCA, IRM acquisition unmixing, and M_{rh} curve PCA results relate to each other. When combined, they provide a clear interpretation of domain state and coercivity distributions for complex magnetic mineral mixtures.

7.3. Advantages and Challenges for Magnetic Unmixing Techniques

Magnetic mineral mixtures generate inevitable difficulties for rock magnetic studies, especially because of the contrast between weak and strong intrinsic magnetizations of hematite and magnetite. In this study, FORC diagrams, FORC-PCA, IRM acquisition curve unmixing, and PCA of hysteresis loops and M_{rh} curves are demonstrated to be valuable for detecting hematite signals and for deciphering complex magnetic mixtures. However, these methods emphasize different aspects of magnetic properties and have their respective strengths and limitations.

FORC diagrams provide diagnostic information about the domain state of magnetic particles and about magnetostatic interactions that are not assessed as reliably with other approaches. A key advantage of the remFORC, iFORC, and tFORC diagrams of Zhao et al. (2017) is that they provide improved domain state specificity for magnetic mineral assemblages with mixed domain states (e.g., Hu et al., 2018; Roberts et al., 2019). For example, sample KA1-1B-1 would usually be interpreted as SD; however, a viscous SP/SD component is highlighted in the remFORC diagram, while the two positive lobes along the B_i axis in the tFORC diagram also confirm a vortex state component (Figures 2b and 2d). For sample KA1-2A-1, we observe both vortex state and SD signals with the conventional FORC diagram, but the negative–positive–negative–positive feature in the iFORC diagram suggests that the low-coercivity component is dominated by vortex state behavior. FORC analyses can be valuable for identifying hematite with large field ranges (Figures 2–4). When dealing with hematite and magnetite mixtures, use of an irregular grid (Zhao et al., 2015) aids efficiency by focusing measurements on regions where the magnetization changes most. This enables capturing of both magnetite and hematite signals with reasonable measurement times and avoiding excessive instrument drift during measurement.

FORC-PCA is a valuable approach for unmixing samples with mixed domain states. The FORC-PCA algorithm of Harrison et al. (2018) performs PCA on local polynomial regression coefficients rather than on the processed FORC diagram, which provides consistent representation of reversible and irreversible components to enable unbiased quantification of MD and viscous SP/SD components. In our analysis, FORC-PCA is more sensitive to ferrimagnetic minerals. PC1, which accounts for 60% of the total variance in the dataset, mainly represents domain state changes in ferrimagnetic minerals. This is because hematite and goethite are less sensitive to domain state change and interactions have less influence because the anisotropy is higher and the spontaneous magnetization is weaker for hematite and goethite compared to magnetite (Muxworthy et al., 2005). Nevertheless, FORC-PCA enables interpretation of FORC behaviors from independent components and provides a better understanding of domain state variations within groups of samples. A single PC may not reflect variations in a single factor; a PC can indicate factors that are affected by the same mechanism or that have the same background, which is valuable for deciphering geological and environmental influences. As is the case for all EM unmixing approaches, individual EMs can represent mixtures and the extent to which such mixed EMs can be separated depends on the parsimony of the adopted interpretation and whether the EM represents a naturally produced mixture that cannot be split apart. Elements of subjectivity exist with EM definition because EM placement can be flexible. The feasibility metrics of Harrison et al. (2018) provide a visual guide for EM selection to keep users from straying into regions where FORCs become physically unrealistic. However, nonunique EMs can give rise to nonunique results. The long measurement times required for FORC measurements also means that they are most likely to be used only for a subset of representative samples.

Decomposition of IRM acquisition or backfield curves enables component-by-component specificity that is not achieved as effectively with other approaches. The principal limitations are the nonuniqueness of solutions and selection of appropriate mathematical functions for fitting (e.g., Roberts et al., 2019). To minimize or avoid nonuniqueness, independent magnetic component identification is needed to provide supervised unmixing (e.g., Heslop, 2015).

M_{rh} PCA has key advantages. First, it only requires hysteresis measurements, which can be made rapidly on large sample sets. Second, the analysis is objective; PCA results indicate the main contributors to remanence

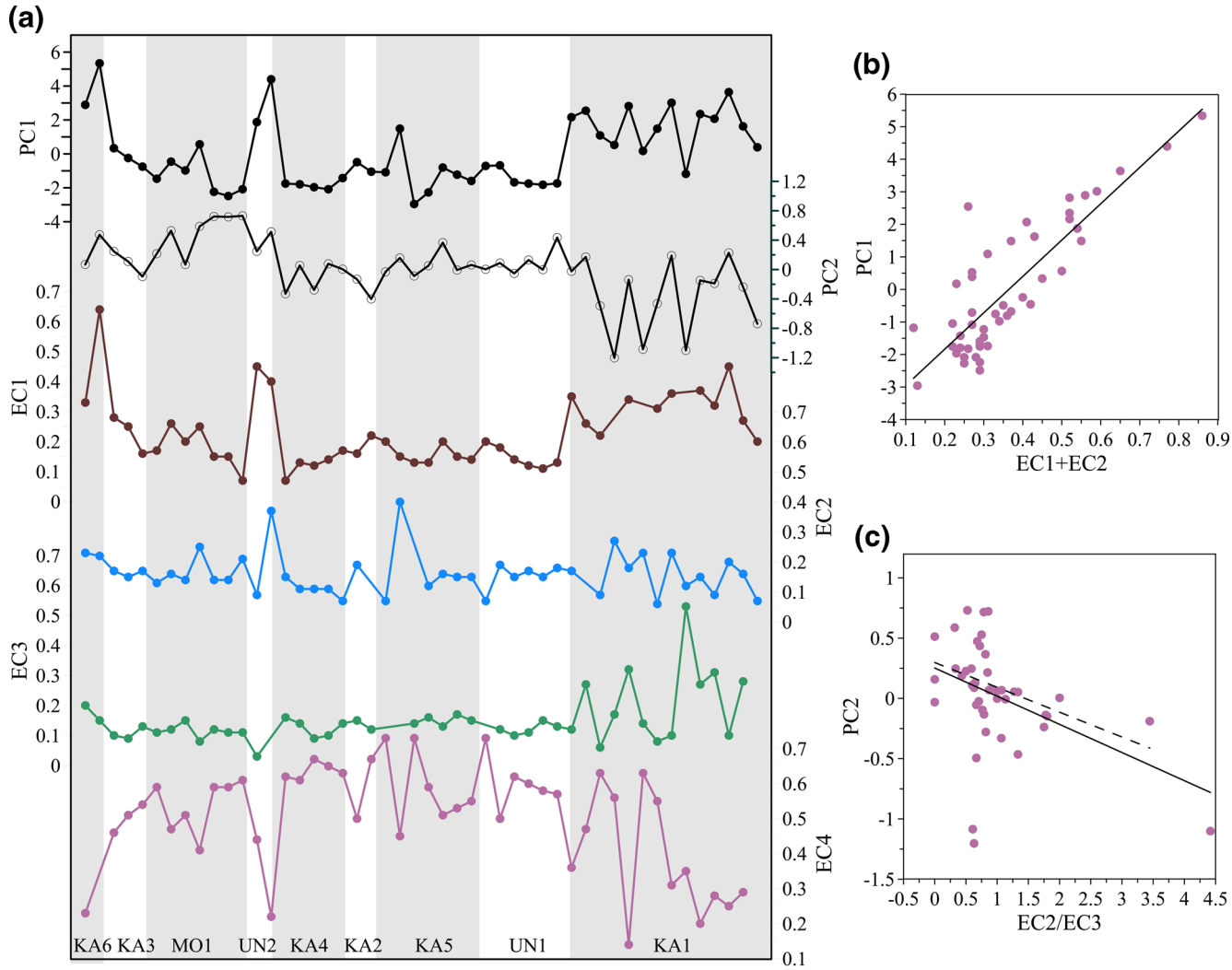

Figure 11. (a) Variation of PC scores from M_{rh} PCA and the contributions of the four magnetic components identified from IRM acquisition unmixing within the red chert samples. Gray bars separate samples from different geological time periods; the horizontal axis represents increasing geological age, where KA6 is the youngest (early Jurassic) and KA1 is the oldest sample (middle Triassic). (b) Relationship between EC1 + EC2 from IRM acquisition unmixing and PC1 from M_{rh} PCA (correlation coefficient $R = 0.85$, $p < 0.001$; this linear correlation is significant at the 0.01 level); (c) weak negative correlation between the PC2 score from M_{rh} curve PCA and the EC2/EC3 value from IRM acquisition unmixing ($R = 0.43$, $p = 0.004$; the correlation is significant at the 0.01 level). The dashed line is a fit without the four points with low-PC2 scores ($R = 0.41$, $p = 0.007$; the correlation is also significant at the 0.01 level).

variations and subtle coercivity changes can be revealed. Unmixing using PCA of M_{rh} and IRM acquisition curves is based on remanent magnetizations. PC1 from M_{rh} PCA follows C1 plus C2 variations from IRM acquisition unmixing (Figures 11a and 11b), which confirms that PC1 represents the relative contribution of low-coercivity and high-coercivity components. PC2 from M_{rh} curve PCA makes a minor contribution to the remanent magnetization, and yet tends to decrease with increasing EC2/EC3 (Figure 11c). This phenomenon indicates that PC2 may be related to the relative abundance of C2 and C3, which could result from mineral input variations or transformation from one component to another. For instance, higher PC2 could represent oxidation of magnetite to hematite resulting in lower C2 but higher C3. Therefore, M_{rh} curve PCA provides reliable and objective coercivity distribution information and connects coercivity components that cannot be retrieved from IRM acquisition curve unmixing. However, M_{rh} curve PCA does not provide direct domain state diagnosis either.

Based on the above results and discussion, for complex magnetite–hematite mixtures, PCA analysis of M_{rh} is recommended for large sample sets to retrieve valuable information on coercivity components and their

interrelations. FORC-PCA provides the best method for domain state unmixing, but it is less sensitive to hematite when magnetite is present. Extended FORC-type diagrams provide unambiguous magnetic domain state diagnosis that is suitable for analysis of selected samples. IRM acquisition curve decomposition provides coercivity-based unmixing, but its subjective and nonunique nature should always be considered when interpreting results.

8. Conclusions

Complex magnetic mineral mixtures in red chert have long been a barrier for making detailed paleomagnetic and environmental magnetic interpretations. Using a combination of IRM acquisition curve unmixing, FORC-PCA unmixing and M_{rh} PCA, we describe an improved approach for discriminating hematite and magnetite in red chert. PCA helps to detect linkages between different magnetite and hematite components. Coarse magnetite varies with hematite, which suggests that they have the same detrital origin while intermediate-coercivity components compete with hematite, which probably indicates an oxidation process or a different formation mechanism for the intermediate-coercivity component.

The usefulness of various magnetic techniques is assessed here for unmixing complex mineral magnetic signals in red cherts. FORC diagrams can enable detection of hematite signals when using larger field ranges and efficient measurement protocols. FORC-PCA is valuable for unmixing domain states. Domain state changes are less important for hematite compared to magnetite; therefore, the usefulness of FORC-PCA is best illustrated with magnetite-dominated samples. IRM acquisition curve and end-member related unmixing provides component-specific results, but they need independent evidence to guide robust end-member selection. PCA on M_{rh} curves enables rapid, objective remanence analysis for large samples sets, which provides useful information about the most significant factors influencing remanence variations and subtle coercivity changes. A FORC diagram contains all information that is contained in a hysteresis loop and IRM curve. It is, therefore, a more diagnostic tool for identifying mineral magnetic components. However, FORCs are sensitive to noise and take longer to measure. Therefore, logistical constraints tend to outweigh the usefulness of this technique for separating magnetic components. When considering magnetically weak natural magnetite–hematite mixtures, such as in the studied red chert, PCA is useful and time efficient. Selective measurement of extended FORC-type diagrams can provide further detailed information on the domain states present.

Data Availability Statement

Dataset is uploaded to the PANGAEA data publisher (https://www.pangaea.de/?t=Geophysics).

Acknowledgments
We thank Ayako Katayama and Emiko Miyamura for their practical assistance to this work. We also thank Xuan Wang for her support to the first author. This work was supported financially by the National Institute of Advanced Industrial Science and Technology, Ministry of Economy, Trade and Industry, Japan (APR, PXH, RJH, DH, ARM, TS, HO, and XZ), the Australian Research Council through grant DP160100805 (APR, RJH, and ARM), and by the European Research Council under the European Union's Seventh Framework Program (FP/2007–2013)/ERC grant agreement number 320750 (RJH).

References

Abrajevitch, A., Hori, R. S., & Kodama, K. (2011). Magnetization carriers and remagnetization of bedded chert. *Earth and Planetary Science Letters*, *305*(1–2), 135–142.

Abrajevitch, A., Hori, R. S., & Kodama, K. (2013). Rock magnetic record of the Triassic-Jurassic transition in pelagic bedded chert of the Inuyama section, Japan. *Geology*, *41*(7), 803–806.

Abrajevitch, A., Pillans, B. J., & Roberts, A. P. (2014). Haematite pigmentation events and palaeomagnetic recording: Implications from the Pilbara Print Stone, Western Australia. *Geophysical Journal International*, *199*(2), 658–672.

Abrajevitch, A., Pillans, B. J., Roberts, A. P., & Kodama, K. (2018). Magnetic properties and paleomagnetism of zebra rock, western Australia: Chemical remanence acquisition in hematite pigment and ediacaran geomagnetic field behavior. *Geochemistry, Geophysics, Geosystems*, *19*(3), 732–748.

Ahmadzadeh, M., Romero, C., & McCloy, J. (2018). Magnetic analysis of commercial hematite, magnetite, and their mixtures. *AIP Advances*, *8*(5), 056807. https://doi.org/10.1063/1.5006474

Ando, A., Kodama, K., & Kojima, S. (2001). Low-latitude and southern hemisphere origin of Anisian (Triassic) bedded chert in the Inuyama area, Mino terrane, central Japan. *Journal of Geophysical Research: Solid Earth*, *106*(B2), 1973–1986. https://doi.org/10.1029/2000JB900305

Bloemendal, J., King, J. W., Hall, F. R., & Doh, S. J. (1992). Rock magnetism of Late Neogene and Pleistocene deep-sea sediments: Relationship to sediment source, diagenetic processes and sediment lithology. *Journal of Geophysical Research: Solid Earth*, *97*(B4), 4361–4375.

Carvallo, C., Muxworthy, A. R., & Dunlop, D. J. (2006). First-order reversal curve (FORC) diagrams of magnetic mixtures: Micromagnetic models and measurements. *Physics of the Earth and Planetary Interiors*, *154*(3), 308–322. https://doi.org/10.1016/j.pepi.2005.06.017

Channell, J. E. T., Harrison, R. J., Lascu, I., McCave, I. N., Hibbert, F. D., & Austin, W. E. N. (2016). Magnetic record of deglaciation using FORC-PCA, sortable-silt grain size, and magnetic excursion at 26 ka, from the Rockall Trough (NE Atlantic). *Geochemistry, Geophysics, Geosystems*, *17*(5), 1823–1841.

Channell, J. E. T., Xuan, C., & Hodell, D. A. (2009). Stacking paleointensity and oxygen isotope data for the last 1.5 Myr (PISO-1500). *Earth and Planetary Science Letters*, *283*(1), 14–23. https://doi.org/10.1016/j.epsl.2009.03.012

Chen, L., Heslop, D., Roberts, A. P., Chang, L., Zhao, X., McGregor, H. V., et al (2017). Remanence acquisition efficiency in biogenic and detrital magnetite and recording of geomagnetic paleointensity. *Geochemistry, Geophysics, Geosystems*, *18*(4), 1435–1450. https://doi.org/10.1002/2016gc006753

Cornell, R. M., & Schwertmann, U. (2004). *The iron Oxides: Structure, Properties, Reactions, Occurences and Uses*. Weinheim, Germany: Wiley-VCH Verlag GmbH & Co. KGaA. https://doi.org/10.1002/3527602097

Deng, C., Shaw, J., Liu, Q., Pan, Y., & Zhu, R. (2006). Mineral magnetic variation of the Jingbian loess/paleosol sequence in the northern Loess Plateau of China: Implications for Quaternary development of Asian aridification and cooling. *Earth and Planetary Science Letters*, *241*(1), 248–259. https://doi.org/10.1016/j.epsl.2005.10.020

Dunlop, D. J., & Özdemir Ö. (1997). *Rock Magnetism: Fundamentals and Frontiers*. Cambridge: Cambridge University Press.

Egli, R. (2003). Analysis of the field dependence of remanent magnetization curves. *Journal of Geophysical Research: Solid Earth*, *108*(B2), 2081. https://doi.org/10.1029/2002JB002023

Egli, R. (2004). Characterization of individual rock magnetic components by analysis of remanence curves, 1. Unmixing natural sediments. *Studia Geophysica et Geodaetica*, *48*(2), 391–446. https://doi.org/10.1023/B:SGEG.0000020839.45304.6d

Egli, R. (2013). VARIFORC: An optimized protocol for calculating non-regular first-order reversal curve (FORC) diagrams. *Global and Planetary Change*, *110*, 302–320.

Fabian, K. (2003). Some additional parameters to estimate domain state from isothermal magnetization measurements. *Earth and Planetary Science Letters*, *213*(3), 337–345. https://doi.org/10.1016/S0012-821X(03)00329-7

Frank, U., & Nowaczyk, N. R. (2008). Mineral magnetic properties of artificial samples systematically mixed from haematite and magnetite. *Geophysical Journal International*, *175*(2), 449–461. https://doi.org/10.1111/j.1365-246X.2008.03821.x

Harrison, R. J., & Feinberg, J. M. (2008). FORCinel: An improved algorithm for calculating first-order reversal curve distributions using locally weighted regression smoothing. *Geochemistry, Geophysics, Geosystems*, *9*(5), Q05016. https://doi.org/10.1029/2008gc001987

Harrison, R. J., Muraszko, J., Heslop, D., Lascu, I., Muxworthy, A. R., & Roberts, A. P. (2018). An improved algorithm for unmixing first-order reversal curve diagrams using principal component analysis. *Geochemistry, Geophysics, Geosystems*, *19*(5), 1595–1610. https://doi.org/10.1029/2018GC007511

Hejda, P., Kapicka, A., Petrovsky, E., & Sjoberg, B. A. (1994). Analysis of hysteresis curves of samples with magnetite and hematite grains. *IEEE Transactions on Magnetics*, *30*(2), 881–883. https://doi.org/10.1109/20.312434

Heslop, D. (2015). Numerical strategies for magnetic mineral unmixing. *Earth-Science Reviews*, *150*, 256–284. https://doi.org/10.1016/j.earscirev.2015.07.007

Heslop, D., Dekkers, M. J., Kruiver, P. P., & Van Oorschot, I. H. M. (2002). Analysis of isothermal remanent magnetization acquisition curves using the expectation-maximization algorithm. *Geophysical Journal International*, *148*(1), 58–64. https://doi.org/10.1046/j.0956-540x.2001.01558.x

Heslop, D., & Dillon, M. (2007). Unmixing magnetic remanence curves without *a priori* knowledge. *Geophysical Journal International*, *170*(2), 556–566. https://doi.org/10.1111/j.1365-246X.2007.03432.x

Heslop, D., & Roberts, A. P. (2012). A method for unmixing magnetic hysteresis loops. *Journal of Geophysical Research: Solid Earth*, *117*(B3), B03103. https://doi.org/10.1029/2011JB008859

Hu, P. X., Zhao, X., Roberts, A. P., Heslop, D., & Rossel, R. A. V. (2018). Magnetic domain state diagnosis in soils, loess, and marine sediments from multiple first-order reversal curve-type diagrams. *Journal of Geophysical Research: Solid Earth*, *123*(2), 998–1017. https://doi.org/10.1002/2017JB015195

Hunt, C. P., Banerjee, S. K., Han, J. M., Solheid, P. A., Oches, E., Sun, W. W., & Liu, T. S. (1995). Rock-magnetic proxies of climate-change in the loess-paleosol sequences of the western loess plateau of China. *Geophysical Journal International*, *123*(1), 232–244. https://doi.org/10.1111/j.1365-246X.1995.tb06672.x

Iwahashi, J., Yoshida, M., Miono, S., Santosh, G., & Santosh, M. (1991). Magnetic microspherules in Permian and Triassic bedded chert from southwest Japan. *Proceedings of the NIPR Symposium on Antarctic Meteorites*, *4*, 420–435.

Jackson, M., & Solheid, P. (2010). On the quantitative analysis and evaluation of magnetic hysteresis data. *Geochemistry, Geophysics, Geosystems*, *11*, Q04Z15. https://doi.org/10.1029/2009GC002932

Jiang, Z. X., Liu, Q. S., Dekkers, M. J., Zhao, X., Roberts, A. P., Yang, Z. Y., et al. (2017). Remagnetization mechanisms in Triassic red beds from South China. *Earth and Planetary Science Letters*, *479*, 219–230.

Jones, D. L., & Murchey, B. (1986). Geologic significance of paleozoic and mesozoic radiolarian Chert. *Annual Review of Earth and Planetary Sciences*, *14*, 455–492.

Kimura, K., & Hori, R. (1993). Offscraping accretion of Jurassic chert-clastic complexes in the Mino-Tamba belt, central Japan. *Journal of Structural Geology*, *15*(2), 145–161. https://doi.org/10.1016/0191-8141(93)90092-O

Kondo, N., & Adachi, M. (1975). Mesozoic strata of the area north of Inuyama, with special reference to the Sakahogi conglomerate. *The Journal of the Geological Society of Japan*, *81*, 373–386.

Kruiver, P. P., Dekkers, M. J., & Heslop, D. (2001). Quantification of magnetic coercivity components by the analysis of acquisition curves of isothermal remanent magnetisation. *Earth and Planetary Science Letters*, *189*(3), 269–276. https://doi.org/10.1016/S0012-821X(01)00367-3

Lagroix, F., & Guyodo, Y. (2017). A new tool for separating the magnetic mineralogy of complex mineral assemblages from low temperature magnetic behavior. *Frontiers in Earth Science*, *5*, 61. https://doi.org/10.3389/feart.2017.00061

Larrasoaña, J. C., Roberts, A. P., Rohling, E. J., Winklhofer, M., & Wehausen, R. (2003). Three million years of monsoon variability over the northern Sahara. *Climate Dynamics*, *21*(7), 689–698. https://doi.org/10.1007/s00382-003-0355-z

Lascu, I., Banerjee, S. K., & Berquó, T. S. (2010). Quantifying the concentration of ferrimagnetic particles in sediments using rock magnetic methods. *Geochemistry, Geophysics, Geosystems*, *11*(8), Q08Z19. https://doi.org/10.1029/2010GC003182

Lascu, I., Harrison, R. J., Li, Y., Muraszko, J. R., Channell, J. E. T., Piotrowski, A. M., & Hodell, D. A. (2015). Magnetic unmixing of first-order reversal curve diagrams using principal component analysis. *Geochemistry, Geophysics, Geosystems*, *16*(9), 2900–2915. https://doi.org/10.1002/2015GC005909

Lee, J. S., Cha, J. M., Yoon, H. Y., Lee, J.-K., & Kim, Y. K. (2015). Magnetic multi-granule nanoclusters: A model system that exhibits universal size effect of magnetic coercivity. *Scientific Reports*, *5*, 12135. https://doi.org/10.1038/srep12135

Liu, P., Hirt, A. M., Schüler, D., Uebe, R., Zhu, P., Liu, T., et al. (2019). Numerical unmixing of weakly and strongly magnetic minerals: Examples with synthetic mixtures of magnetite and hematite. *Geophysical Journal International*, *217*(1), 280–287. https://doi.org/10.1093/gji/ggz022

Liu, Q., Banerjee, S. K., Jackson, M. J., Zhu, R., & Pan, Y. (2002). A new method in mineral magnetism for the separation of weak antiferromagnetic signal from a strong ferrimagnetic background. *Geophysical Research Letters*, *29*(12), 1565. https://doi.org/10.1029/2002GL014699

Lowrie, W. (1990). Identification of ferromagnetic minerals in a rock by coercivity and unblocking temperature properties. *Geophysical Research Letters*, *17*(2), 159–162. https://doi.org/10.1029/GL017i002p00159

Maher, B. A. (1988). Magnetic properties of some synthetic sub-micron magnetites. *Geophysical Journal International*, *94*(1), 83–96. https://doi.org/10.1111/j.1365-246X.1988.tb03429.x

Matsuo, M., Kubo, K., & Isozaki, Y. (2002). *Mössbauer Spectroscopic Study on Characterization of Iron in the Permian to Triassic Deep-Sea Chert from Japan*. Dordrecht, Netherlands: Springer.

Maxbauer, D. P., Feinberg, J. W., & Fox, D. L. (2016). MAX UnMix: A web application for unmixing magnetic coercivity distributions. *Computers & Geosciences*, *95*, 140–145. https://doi.org/10.1016/j.cageo.2016.07.009

Maxbauer, D. P., Feinberg, J. M., Fox, D. L., & Nater, E. A. (2017). Response of pedogenic magnetite to changing vegetation in soils developed under uniform climate, topography, and parent material. *Scientific Reports*, *7*(1), 17575. https://doi.org/10.1038/s41598-41017-17722-41592

Muxworthy, A. R., King, J. G., & Heslop, D. (2005). Assessing the ability of first-order reversal curve (FORC) diagrams to unravel complex magnetic signals. *Journal of Geophysical Research: Solid Earth*, *110*(B1), B01105. https://doi.org/10.1029/2004JB003195

Nakada, R., Ogawa, K., Suzuki, N., Takahashi, S., & Takahashi, Y. (2014). Late Triassic compositional changes of aeolian dusts in the pelagic Panthalassa: Response to the continental climatic change. *Palaeogeography, Palaeoclimatology, Palaeoecology*, *393*, 61–75. https://doi.org/10.1016/j.palaeo.2013.10.014

Oda, H., & Suzuki, H. (2000). Paleomagnetism of Triassic and Jurassic red bedded chert of the Inuyama area, central Japan. *Journal of Geophysical Research: Solid Earth*, *105*(B11), 25743–25767.

Ouyang, T., Heslop, D., Roberts, A. P., Tian, C., Zhu, Z., Qiu, Y., et al. (2014). Variable remanence acquisition efficiency in sediments containing biogenic and detrital magnetites: Implications for relative paleointensity signal recording. *Geochemistry, Geophysics, Geosystems*, *15*(7), 2780–2796. https://doi.org/10.1002/2014gc005301

Özdemir, Ö., & Dunlop, D. J. (2014). Hysteresis and coercivity of hematite. *Journal of Geophysical Research: Solid Earth*, *119*(4), 2582–2594. https://doi.org/10.1002/2013jb010739

Paterson, G. A., Zhao, X., Jackson, M., & Heslop, D. (2018). Measuring, processing, and analyzing hysteresis data. *Geochemistry, Geophysics, Geosystems*, *19*(7), 1925–1945. https://doi.org/10.1029/2018GC007620.16/j.epsl.2013.09.031

Pike, C. R., Roberts, A. P., & Verosub, K. L. (1999). Characterizing interactions in fine magnetic particle systems using first order reversal curves. *Journal of Applied Physics*, *85*(9), 6660–6667. https://doi.org/10.1063/1.370176

Rivas, J., Zamarro, J., Martin, E., & Pereira, C. (1981). Simple approximation for magnetization curves and hysteresis loops. *IEEE Transactions on Magnetics*, *17*(4), 1498–1502. https://doi.org/10.1109/TMAG.1981.1061241

Roberts, A. P., Chang, L., Heslop, D., Florindo, F., & Larrasoaña, J. C. (2012). Searching for single domain magnetite in the "pseudo-single-domain" sedimentary haystack: Implications of biogenic magnetite preservation for sediment magnetism and relative paleointensity determinations. *Journal of Geophysical Research: Solid Earth*, *117*(B8), B08104. https://doi.org/10.1029/2012jb009412

Roberts, A. P., Cui, Y., & Verosub, K. L. (1995). Wasp-waisted hysteresis loops: Mineral magnetic characteristics and discrimination of components in mixed magnetic systems. *Journal of Geophysical Research: Solid Earth*, *100*(B9), 17909–17924. https://doi.org/10.1029/95JB00672

Roberts, A. P., Florindo, F., Chang, L., Heslop, D., Jovane, L., & Larrasoaña, J. C. (2013). Magnetic properties of pelagic marine carbonates. *Earth-Science Reviews*, *127*, 111–139. https://doi.org/10.1016/j.earscirev.2013.09.009

Roberts, A. P., Hu, P. X., Harrison, R. J., Heslop, D., Muxworthy, A. R., Oda, H., et al. (2019). Domain state diagnosis in rock magnetism: Evaluation of potential alternatives to the Day diagram. *Journal of Geophysical Research: Solid Earth*, *124*, 5286–5314. https://doi.org/10.1029/2018jb017049

Roberts, A. P., Pike, C. R., & Verosub, K. L. (2000). First-order reversal curve diagrams: A new tool for characterizing the magnetic properties of natural samples. *Journal of Geophysical Research: Solid Earth*, *105*(B12), 28461–28475. https://doi.org/10.1029/2000jb900326

Roberts, A. P., Zhao, X., Harrison, R. J., Heslop, D., Muxworthy, A. R., Rowan, C. J., et al. (2018). Signatures of reductive magnetic mineral diagenesis from unmixing of first-order reversal curves. *Journal of Geophysical Research: Solid Earth*, *123*(6), 4500–4522. https://doi.org/10.1029/2018jb015706

Robertson, D. J., & France, D. E. (1994). Discrimination of remanence-carrying minerals in mixtures, using isothermal remanent magnetisation acquisition curves. *Physics of the Earth and Planetary Interiors*, *82*(3), 223–234. https://doi.org/10.1016/0031-9201(94)90074-4

Shibuya, H., & Sasajima, S. (1986). Paleomagnetism of red cherts—A case-study in the Inuyama Area, central Japan. *Journal of Geophysical Research: Solid Earth*, *91*(B14), 14105–14116.

Tauxe, L., Mullender, T. A. T., & Pick, T. (1996). Potbellies, wasp-waists, and superparamagnetism in magnetic hysteresis. *Journal of Geophysical Research: Solid Earth*, *101*(B1), 571–583. https://doi.org/10.1029/95JB03041

Valet, J.-P., Meynadier, L., & Guyodo, Y. (2005). Geomagnetic dipole strength and reversal rate over the past two million years. *Nature*, *435*(7043), 802–805. https://doi.org/10.1038/nature03674

Von Dobeneck, T. (1996). A systematic analysis of natural magnetic mineral assemblages based on modelling hysteresis loops with coercivity-related hyperbolic basis functions. *Geophysical Journal International*, *124*(3), 675–694.

Wuertz, D., & Chalabi, Y. (2015). *Package 'fGarch': Rmetrics—Autoregressive Conditional Heteroskedastic Modelling*. R Package Version 3010.82. https://cran.r-project.org/web/packages/fGarch/fGarch.pdf

Yamazaki, T., & Oda, H. (2005). A geomagnetic paleointensity stack between 0.8 and 3.0 Ma from equatorial Pacific sediment cores. *Geochemistry, Geophysics, Geosystems*, *6*(11), Q11H20. https://doi.org/10.1029/2005gc001001

Zhao, X., Heslop, D., & Roberts, A. P. (2015). A protocol for variable-resolution first-order reversal curve measurements. *Geochemistry, Geophysics, Geosystems*, *16*(5), 1364–1377. https://doi.org/10.1002/2014gc005680

Zhao, X., Roberts, A. P., Heslop, D., Paterson, G. A., Li, Y., & Li, J. (2017). Magnetic domain state diagnosis using hysteresis reversal curves. *Journal of Geophysical Research: Solid Earth*, *122*(7), 4767–4789. https://doi.org/10.1002/2016JB013683

Zhao, X. Y., Fujii, M., Suganuma, Y., Zhao, X., & Jiang, Z. (2018). Applying the Burr type XII distribution to decompose remanent magnetization curves. *Journal of Geophysical Research: Solid Earth*, *123*, 8298–8311. https://doi.org/10.1029/2018JB016082

Ziegler, L. B., Constable, C. G., Johnson, C. L., & Tauxe, L. (2011). PADM2M: A penalized maximum likelihood model of the 0–2 Ma palaeomagnetic axial dipole moment. *Geophysical Journal International*, *184*(3), 1069–1089. https://doi.org/10.1111/j.1365-246X.2010.04905.x